3-Dimensional insight into zonation within slag rims of aged blended cement

Zhang, Yu; Çopuroğlu, Oğuzhan

DOI
10.1016/j.cemconres.2023.107396

Publication date
2023

Document Version
Final published version

Published in
Cement and Concrete Research

Cement and Concrete Research 176 (2024) 107396

Contents lists available at ScienceDirect

Cement and Concrete Research

journal homepage: www.elsevier.com/locate/cemconres

3-Dimensional insight into zonation within slag rims of aged blended cement

Yu Zhang [a,b,*], Oğuzhan Çopuroğlu [b]

[a] Key Laboratory of Concrete and Prestressed Concrete Structures of the Ministry of Education, Southeast University, Nanjing, 210096, China
[b] Microlab, Section of Materials and Environment, Faculty of Civil Engineering and Geosciences, Delft University of Technology, Delft, the Netherlands

ARTICLE INFO

Keywords:
Slag rim
Zonation
SEM and TEM
3-Dimensional
Slag grain size

ABSTRACT

Through the integration of SEM-BSE and TEM, we gained a comprehensive 3-dimensional understanding of different distribution patterns of inner hydration products of slag. For fully hydrated small slag grains, two distinct sub-zones were formed in the rims. Lath-like, well-crystalline hydrotalcite-like crystals were found to precipitate, grow, and accumulate near the boundary, forming a layer with a thickness slightly exceeding 0.5 μm. In the center, entrapped calcium and silicon played roles in the formation of a homogeneous and fibrous C–(A)–S–H gel phase. The concentration equilibrium between cement matrix and grain core led to the establishment of a similar grey pixel value and Ca/Si atomic ratio of gel phase at ~1.10. As the size of slag grains increased, three sub-zones became visible. Hydrotalcite-like phase was enriched near the boundary, followed by a sandwiched area abundant in C–(A)–S–H gel phase. Due to the low mobility and increased migration distance, newly released magnesium from reaction front accumulated locally to form a new Mg-rich region.

1. Introduction

Blast furnace slag, referred to as *slag* in this paper, is the waste generated during the production of pig iron. In the blast furnace, raw iron ore gangues, reduced substances, and melted coke components are mixed together, resulting in the formation of liquid slag at a temperature of approximately 1450 °C. [1]. The main constituents of slag are calcium oxide and silica, which are present in significant quantities. Additionally, it contains certain amounts of alumina and magnesia. Thus, it is commonly described as a $CaO–SiO_2–Al_2O_3–MgO$ quaternary system. Additionally, trace constituents such as neighboring alkalis (Na and K) and sulfur compounds are also absorbed by the slag [2]. Upon rapid cooling using powerful water jets, the molten/liquid slag solidifies instantly, turning into a granular and nearly fully glassy form. In most cases, after proper grinding, slag is adopted as a supplementary cementitious material (SCM) for cement and concrete productions [3,4].

To produce strength-building hydration products, slag needs to be activated [5]. This is different from hydraulic binders like Ordinary Portland cement, which can react with water directly. The stimulator can be NaOH/water glass solution found in alkali-activated slag paste or portlandite, generated when cement clinkers hydrate and therefore is available in blended cements.

In general, the hydration of a single slag particle in an alkaline environment typically follows a dissolution-precipitation-diffusion mechanism [6]. At early age, the process is determined by the dissolution-precipitation mechanism [7,8]. As the reaction progresses and unreacted slag grains become covered by reaction products, ion diffusion takes control and governs its continuous hydration [9].

Regarding the hydration products of slag, secondary precipitations including calcium silicate hydrate and Mg—Al hydrotalcite-like phase have been identified [10]. These hydrates are known to precipitate only within the original area of the slag, creating a mixture referred to as the 'inner' hydration products of slag, sometimes also termed as '*slag rim*'. A relatively fine-textured inner products were observed by Transmission Electron Microscope (TEM) in the slag-containing systems [11–15]. Hydrotalcite-like phase exhibited a plate- or lath-like nano-morphology [11,15]. As for the distribution pattern of hydrates within slag rims, contradictory views do exist in the literature. Through Scanning Electron Microscope (SEM) and TEM, Ye [16] argued that the negatively-charged C–(A)–S–H gel phase layers were strongly attracted to the positively-charged hydrotalcite-like phase layers in the rims. However, instead of intermixture, the work in [17] illustrated that three distinct

* Corresponding author at: Key Laboratory of Concrete and Prestressed Concrete Structures of the Ministry of Education, Southeast University, Nanjing 210096, China.
E-mail address: 101013462@seu.edu.cn (Y. Zhang).

https://doi.org/10.1016/j.cemconres.2023.107396
Received 16 July 2023; Received in revised form 23 November 2023; Accepted 26 November 2023
Available online 30 November 2023

sub-zones were formed around unreacted slag grains, i.e., Mg—Al hydrotalcite-like phase, C–(A)–S–H gel phase, and Ca – Al layered double hydroxide phase. In our previous work [18], it was concluded that different distribution patterns of inner hydration products can be identified depending on the original grain sizes of slag.

Note that existing studies concentrating on slag particles in cementitious systems are restricted to periods up to several years, at most. During this curing age, most (large) slag particles are far from reaching their full potential with respect to hydration degree. Particularly for samples with a short-term curing age, the formed rims around unreacted slag cores are too thin to allow for accurate analysis. Besides, for all microscopical techniques employed for imaging, only a 2-dimensional view can be provided of a 3-dimensional microstructure. Thus, misleading conclusions may be summarized, as demonstrated in [19].

Building upon the research conducted in [18], the present study examined these 40-year-old slag cement concrete samples further. The slag grains in the samples were categorized into three groups based on their apparent original diameters or sizes, i.e., small (< 8 μm), medium (8–17 μm), and large (> 15 μm). For each class, representative slag grains were selected and analyzed in the following 3.1 to 3.3 sections correspondingly. During the analysis, the authors extended 2-dimensional SEM imaging to multiple SEM-BSE (sample surface) and in-situ TEM (vertical section beneath the surface) observations, to explore the distribution patterns of hydrates within the slag rims in a three-dimensional manner. Furthermore, in the discussion section, a schematic illustration of the 3-dimensional distribution patterns of hydrates in the slag rims was present, along with a detailed comparison of them. The misleading results based on 2-dimensional view were also illustrated and explained 3-dimensionally. Overall, the findings obtained this paper provided valuable insights into the zonation within slag rims, including the morphology and composition of each sub-zone, as well as the various distribution patterns depending on the size of the original slag grains.

2. Materials and methodology

2.1. Sample information

The field concrete samples were extracted from the Rozenburg Wind Wall in 2021. This particular concrete structure was situated between Road Isarweg and Neckarweg, in the Europoort Rotterdam, Netherlands. It was originally constructed using CEM III/B in 1985. For the hydration products of these samples, readers can refer to the Fig. 1 in [18].

2.2. Experimental methods

Initially, the selected samples were immersed in an isopropanol solution for one week (refreshed every two days) to terminate reaction, dried in a 40 °C oven for several minutes, and then impregnated with epoxy resin. Subsequently, the hardened surfaces were ground and polished in turn to achieve a smooth finish. These well-polished sample surfaces were finally carbon coated using a Leica EM CED030 carbon evaporator for the following micro- and nano-analysis.

2.2.1. SEM

To obtain back-scattered electron (BSE) image, the prepared samples were characterized by a FEI QUANTA FEG 650 ESEM under a high vacuum chamber condition. The working distance and accelerating voltage utilized were kept at 10 mm and 10 kV, respectively. A typical area of different heights was examined under the same instrumental conditions to obtain multiple observations (as shown in Fig. 1). This study involved three observations under back-scattered mode, resulting in the acquisition of three cross-sections of slag grains. This approach enabled the viewing of their rims in a 3-dimensional manner.

2.2.2. FIB-SEM-TEM

Moreover, polished surfaces were loaded into a dual-beam FIB-SEM system (Zeiss Crossbeam 540) to precisely navigate slag rims of interest for in-situ TEM observations. Focused ion beam (FIB) technology was adopted to prepare a microscopic section for TEM characterization through sputtering and milling. A schematic illustration of the sample preparation process is introduced in Fig. 2. Firstly, the target area, which was a thick rim along a partially hydrated slag grain (as marked in Fig. 2 (b)), was located through SEM under back-scattered mode. Following, this region was coated with platinum on the surface, as Fig. 2 (c) exhibits. The matrix on both sides of the platinum cover was slowly cut with focused Ga^+ ion beam (Fig. 2 (d)). Subsequently, the section beneath the cover was extracted from the matrix (Fig. 2 (e)) and transferred to a Cu support (Fig. 2 (f)) for further operations. As Fig. 2 (g) shows, focused Ga^+ ion was further utilized to thin the extracted slice down to a thickness of about 100 nm (Fig. 2 (h)). One should keep in mind that due to the brittleness of cement matrix, the accelerated voltage and beam density of focused Ga^+ ion beam should be maintained as low as possible (~5 kV, depending on the strength of cement matrix), to minimize the damage caused by the milling process.

Finally, the nano-scale morphology and elemental composition of a cross-section perpendicular to the sample surface were analyzed by means of a FEI talos F200X G2 in tandem with a high-angle annular dark-field detector (HAADF) and an X-ray energy dispersive detector. Combining the analysis for surface (SEM) and vertical section beneath the surface (TEM), the hydrates in the target rims can be reconstructed 3-dimensionally.

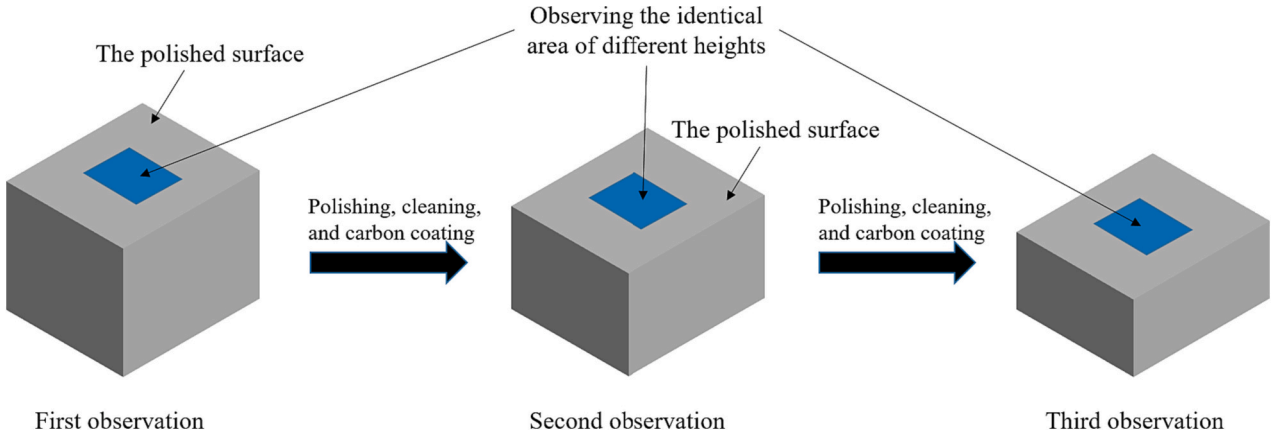

Fig. 1. Schematic illustration of sample preparation for multiple SEM-BSE observations.

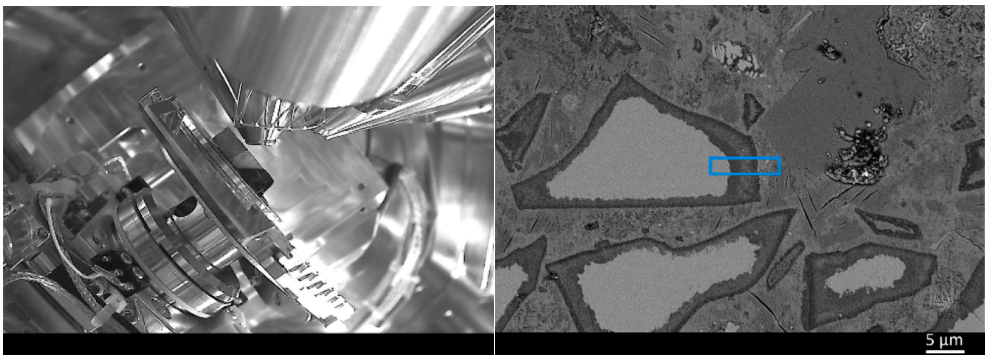

(a) Loading the sample (b) Target area (blue box)

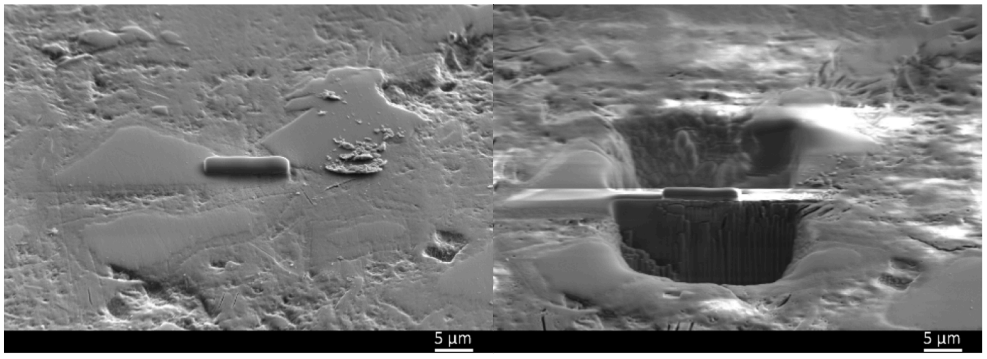

(c) Coating with platinum as cover (d) Cutting the matrix

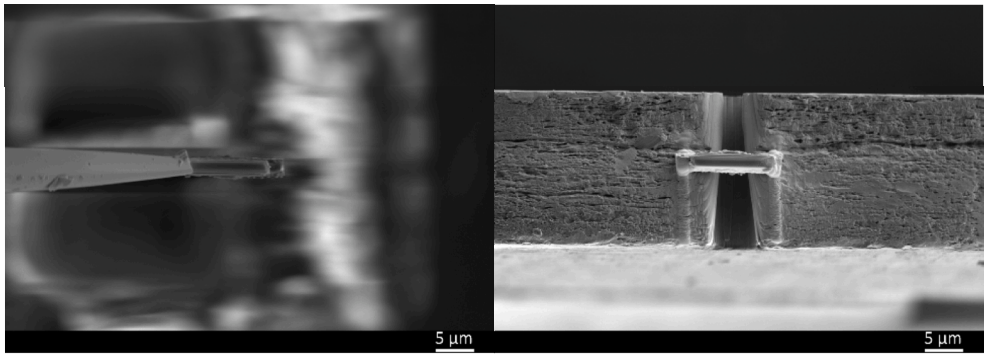

(e) Extracting the section (f) Placing on a Cu support

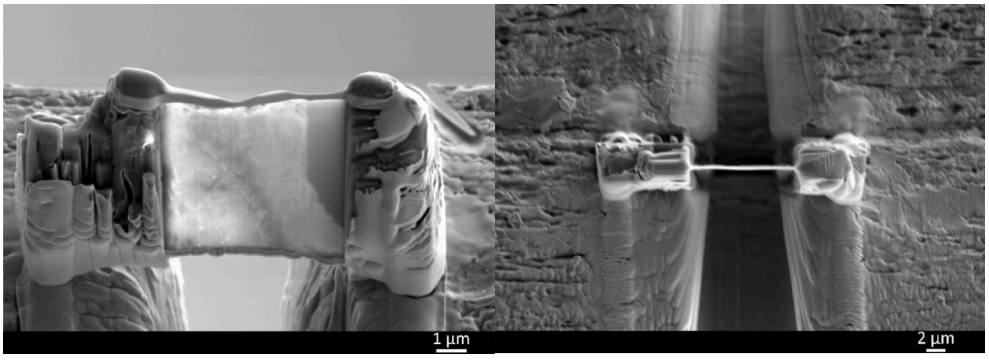

(g) Milling for TEM analysis (h) Top view after milling

Fig. 2. Schematic sample preparation for in-situ TEM observations using a dual-beam FIB-SEM system.

3. Results

3.1. Small slag grains

In Fig. 3, a dense cement matrix can be observed, with unreacted slag grains incorporated. Inner hydration products were found to precipitate as rims along partially hydrated slag particles. For fully hydrated small slag grains (indicated by white circles), two distinctive sub-zones can be distinguished within the original slag perimeter. The border displayed a relatively dark coloration while the center showed a relatively grey pixel value, almost the same coloration to cement matrix. Considering the possible elements existing in the blended system (Ca, Si, Al, and Mg) and their corresponding mean atomic numbers, magnesium was believed to accumulate near the boundary, whereas calcium and silicon were enriched in the core. On the other hand, for the areas highlighted by green circles, they also appeared to belong to the small group based on their acquired sizes; however, no clear zonation was seen, as Mg seemed to occupy the entire region.

3.1.1. Multiple SEM-BSE observations

To overcome the main limitation of microscopical imaging that only 2-dimensional section of a 3-dimensional microstructure were observed, three representative zones were chosen for multiple SEM-BSE observations. Specifically, three observations were undertaken for each of them, as illustrated in Fig. 4.

In circle 1, three small slag particles with similar coloration characteristics to those white-circled in Fig. 3 eventually disappeared after three times of polishing. As for the two grains circled as 2, different phenomenon occurred with polishing. The left one also faded away gradually. However, the right grain, which presented similar features to those green-circled in Fig. 3, its apparent size increased notably after the third polishing. It was evident that this area did not originate from a totally reacted small slag grain. Instead, it was cut from the rim of a larger slag grain.

3.1.2. In-situ observations with TEM

In order to gain a more in-depth insight of the two distinct phenomena described above, TEM was utilized to exhibit the morphology and composition of inner hydrates at a nano-scale level. Specifically, two typical examples, one with and the other without magnesium in the core, were selected for individual analysis in the subsequent section.

3.1.2.1. Without Mg in the core. The target area, indicated by the rectangle in Fig. 5 (a), was adopted as an example of slag particle without Mg in the core. It was worth noting that this small slag grain exhibited similar characteristics to those white-circled in Fig. 3 and encircled as 1 in Fig. 4, i.e., the center displayed the same coloration as the surrounding matrix.

Fig. 3. A representative BSE micrograph of the microstructure.

Fig. 5 (c) illustrates the overall morphology of vertical section, taken beneath the platinum cover and perpendicular to the surface. A clear border was observed, separating the inner and outer products of slag grain. A magnified image of the selected area was elaborated in Fig. 5 (d). For the outer products, a generally homogeneous, dense, and fibrous morphology was noted in the region marked as P1 (Fig. 5 (e)). These characteristics aligned with the typical features of C−(A)–S–H gel phase [11–14]. Additionally, the absence of discernible diffraction spot in Fig. 5 (e-1) verified that gel phase formed in this region was disordered.

Zooming in on the interface between the outer and inner products, i.e., the initial boundary of the slag grain (P2), a magnified image was displayed in Fig. 5(f). These well-crystalline phases, exhibiting an inward growth direction, primarily manifested as a distinct lath-like morphology. Undoubtedly, they corresponded to the massive precipitation of hydrotalcite-like crystals [11,15,17]. Fringes, as can be seen in Fig. 5 (f-1) and (f-2), were indicative of the ordered stacking of atomic planes in this crystal. Moreover, clear diffraction spots were detected in the fast Fourier transform (FFT) pattern in Fig. 5 (f-3). The average basal spacing of 0.7542 ± 0.0022 nm, 0.3755 ± 0.0034 nm, and 0.2516 ± 0.0013 nm (measured from the inverse fast Fourier transform (IFFT) pattern) corresponded to the plane R1, R2, and R3, respectively. According to TEM point analysis, its Mg/Al atomic ratio was ~2.02. These values matched well with the $d_{(003)}$, $d_{(006)}$, and $d_{(009)}$ parameters of hydrotalcite $Mg_4Al_2(OH)_{14}{\cdot}3H_2O$ (PDF: 0035–0964).

When approaching the middle (P3), another homogeneous and fibrous morphology of hydration products was detected (Fig. 5 (g)). The absence of diffraction spot (Fig. 5 (g-1)) confirmed the formation of disordered C−(A)–S–H gel phase in the center. Meanwhile, it was noticed that the nanostructure of gel phase in the core was relatively more porous compared to that as outer products. However, TEM point analysis revealed similar Ca/Si and Al/Si atomic ratios for C−(A)–S–H gel phase as both inner and outer products, at ~1.10 and ~ 0.17 respectively. These values were consistent with the findings reported in [11].

In Fig. 6, the elemental mappings (Ca, Si, Al, and Mg) of a typical region containing both outer and inner products of slag are provided. In agreement with the morphology observed in Fig. 5, aluminum and magnesium species were found to accumulate near the boundary for the precipitation of hydrotalcite-like crystal. The core, on the other hand, was rich in calcium and silicon, deficient in aluminum, and without any trace of magnesium. As such, it was mainly composed of highly disordered C−(A)–S–H gel phase.

3.1.2.2. With Mg in the core. As shown in Fig. 7 (a), Mg was evenly distributed throughout the whole target area, similar to the green-circled regions in Fig. 3. There was no evidence of any remaining slag remnant inside the perimeter, which could lead to the mistaken assumption of complete hydration of a small slag grain. Interestingly, unlike the case discussed in Section 3.1.2.1, no clear variation in coloration was noted between the boundary and core regions.

Fig. 7 (c) gives an overview of the vertical section of the target area. Similarly, a clear border distinguished the inner and outer products of slag grain. A closer look at the selected region was shown in Fig. 7 (d). The outer products, which primarily consisted of C−(A)–S–H gel phase, exhibited a homogeneous and fibrous morphology in the area labelled as P1 (Fig. 7 (e)). Within the rim, three sub-zones with hydrates presenting intrinsic differences in morphology can be identified. In the magnified image of the initial boundary (P2) displayed in Fig. 7 (f), amounts of hydrotalcite-like crystals grew inwards and presented a lath-like morphology (Fig. 7 (f-1)). Fringes, implying the layered structure of this phase, were marked in Fig. 7 (f-2). When moving inside further, a fibrous morphology of the hydration products reappeared in the bottom-right corner of Fig. 7 (g), and a zoomed in image was provided in Fig. 7

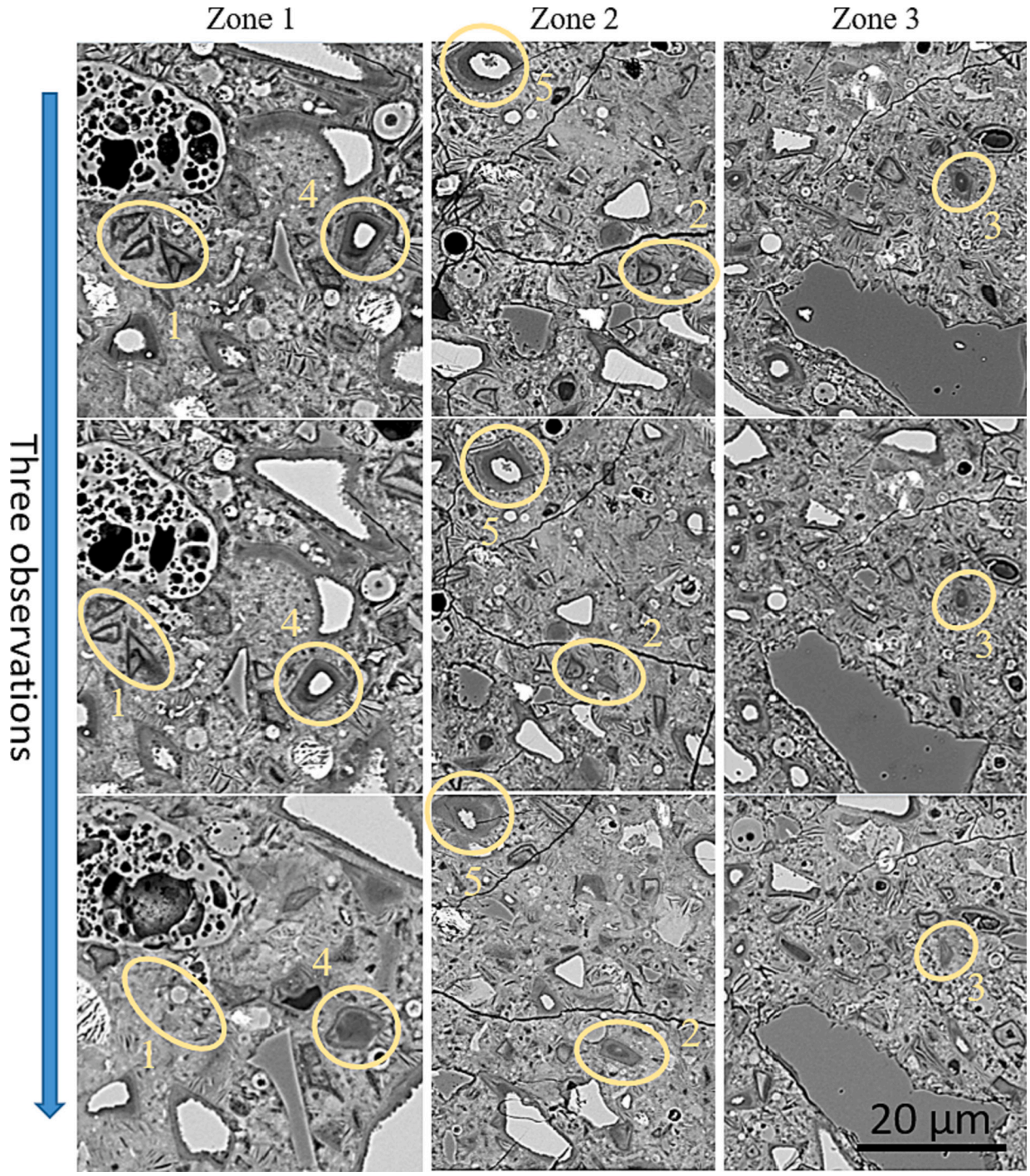

Fig. 4. Three typical zones for multiple SEM-BSE observations.

(g-1). It verified the precipitation of C–(A)–S–H gel phase adjacent to the hydrotalcite-like phase.

In comparison to the case discussed in Section 3.1.2.1, the main difference occurred in the center region where P3 was located. A coarse and rough texture was found here (Fig. 7 (g)). The analysis of this specific sub-zone would be further explored in the discussion section. In fact, slag rim with three sub-zones was originated from a medium/large grain (see Sections 3.2 and 3.3), rather than a small one.

Fig. 8 depicts the HAADF micrograph and main element mappings of the highlighted area in Fig. 7 (c). Magnesium specie occupied the whole region, although its concentration seemed to gradually decrease towards the interior. Deficiency of calcium and silicon was noticed near the boundary, suggesting that most Ca and Si ions dissolved had migrated into the surrounding matrix. As for aluminum, it was distributed evenly across the entire area.

Combining the results of multiple SEM-BSE and in-situ TEM observations together, it can be concluded that for small slag grains after full hydration, they typically presented a zonation with two intrinsically different sub-zones, i.e., a lath-like hydrotalcite-like phase near the border and a fibrous C–(A)–S–H gel phase in the core. As for cases grouped into small class (based on apparent size) while with Mg in the core, they were actually sections cut from rims of medium or large slag grains.

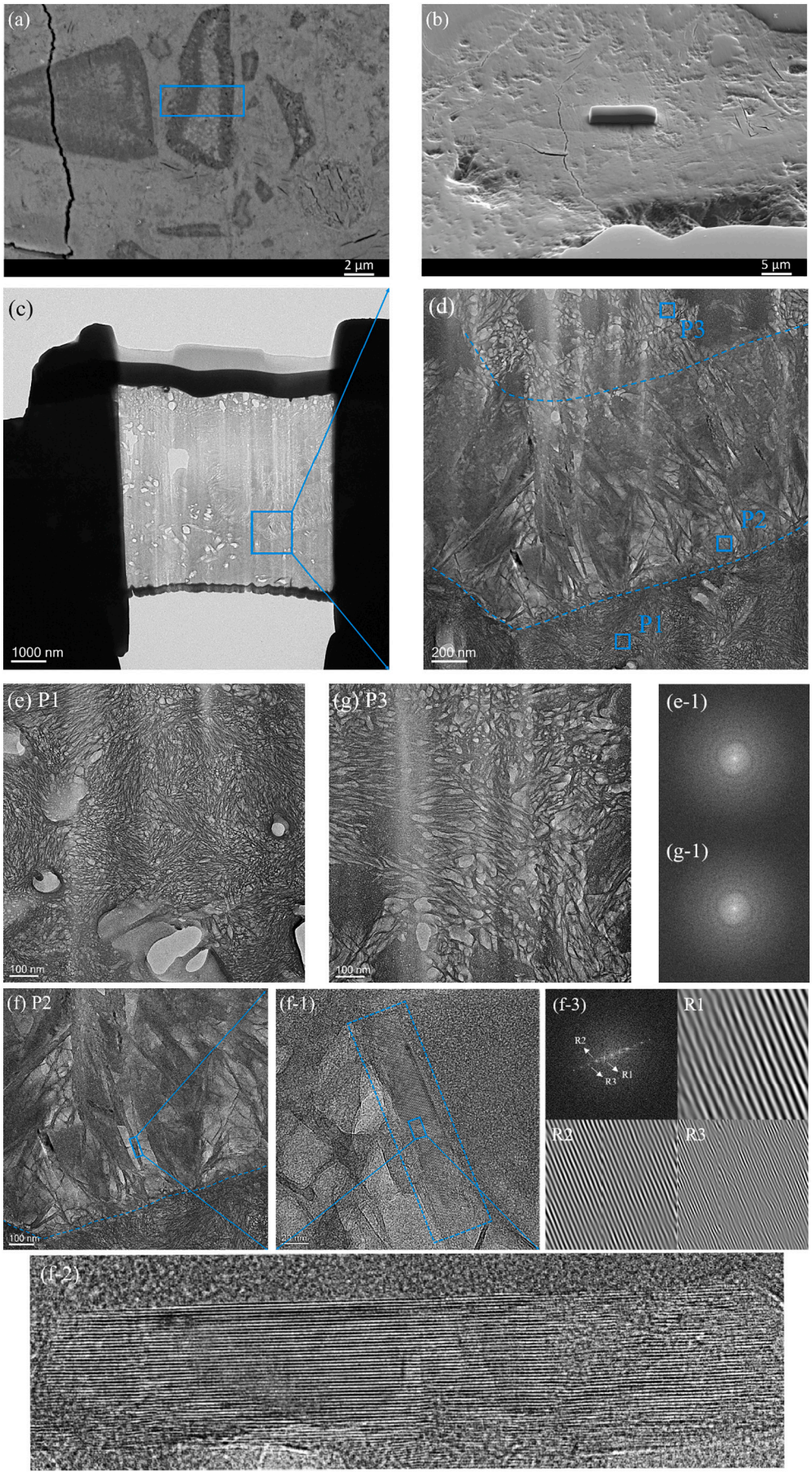

(caption on next page)

Fig. 5. TEM analysis of hydrates in the rim of a totally hydrated small slag grain; (a) BSE image of the target area; (b) Coating the area with platinum cover; (c) The overall morphology of vertical section of the target area; (d) Magnified image of the area marked in (c); (e) Magnified image of the area marked as P1 in (d); (e-1) The fast Fourier transform of phases in this region; (f) Magnified image of the area marked as P2 in (d); (f-1) High resolution lattice fringe image of the phase marked in (f); (f-2) Zoomed in image of the squared region indicated in (f-1); (f-3) The fast Fourier transform and inverse fast Fourier transform of phases in (f-2); (g) Magnified image of the area marked as P3 in (d); (g-1) The fast Fourier transform of phases in this region.

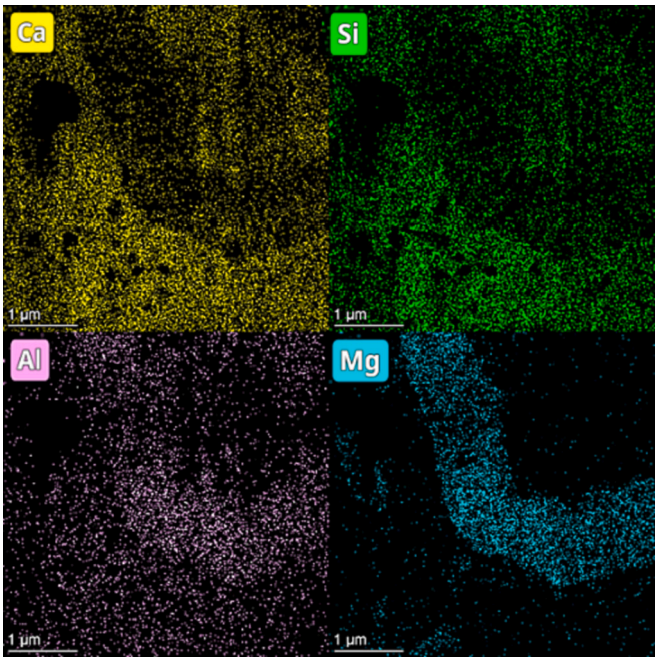

Fig. 6. Elemental mappings (Ca, Si, Al, and Mg) of a typical region containing both outer and inner products of slag.

3.2. Medium slag grains

As red-circled in Fig. 9, three sub-zones can be seen in the fully hydrated medium grains with two distinct grey pixel values. The area near the boundary as well as grain core exhibited a dark coloration with a lower average atomic number, implying the presence of magnesium in these two regions. In contrast, the area in-between (named as sandwiched zone henceforth) where calcium was abundant, presented a less dark coloration with a higher mean atomic number.

3.2.1. Multiple SEM-BSE observations

During multiple SEM-BSE observations, several interesting phenomenon occurred. For example, the reacted medium slag particle encircled as 3 in Fig. 4 showed three sub-zones in the rim, and its apparent size gradually reduced with repeated polishing. Besides, these sub-zones were expected to vanish if further polishing was implemented. However, this elemental distribution pattern can also be originated from a partially hydrated large slag grain, as observed in circle 4.

3.2.2. In-situ observations with TEM

Next, TEM was utilized to elucidate the morphology and composition of this elemental distribution pattern at a nano-scale level. The area of interest was indicated by the rectangle in the BSE micrograph of Fig. 10 (a). Three sub-zones were detected to form in the rim, distinguished by two grey pixel values.

Fig. 10 (c) presents the overall morphology of target area beneath the platinum cover. The border between inner and outer products of slag grain was noticed clearly. A zoomed in image of the selected area was displayed in Fig. 10 (d). In the lower part of area marked as P1 (Fig. 10 (e)), fibrous C−(A)–S–H gel phase belonging to the outer products was noted. Close to the initial boundary (P2), numbers of hydrotalcite-like crystals were detected, exhibiting an inward growth direction and a lath-like morphology (Fig. 10 (f)). Its layered structure was suggested by the fringes occurred in Fig. 10 (f-1). Moving inside to the sandwiched zone (P3), fibrous morphology of the hydration products was found again (Fig. 10 (g)).

When approaching the area labelled as P4, a rough texture was detected surrounding the unhydrated grain core (Fig. 10 (h)), like the case examined in Section 3.1.2.2. According to the results of linescan and element mapping in Fig. 11 and 12 respectively, magnesium accumulated here to form a new Mg-rich region, representing the dark core in Fig. 10 (a). Nonetheless, no lath-like morphology indicating the formation of hydrotalcite-like crystal was observed in this sub-zone. In addition, no diffraction spot was seen in the fast Fourier transform pattern in Fig. 10 (h-1).

It should be noted that no trace of an unreacted core was detected in the BSE image; however, some remnant particles were recognized beneath the surface, e.g., the right part in Fig. 10 (h) which presented an opaque feature. This observation aligned with the findings from multiple SEM-BSE observations in Section 3.2.1, confirming that the observed elemental distribution pattern can also be sourced from the thick rim of a partially hydrated large slag grain.

Fig. 11 reports the EDS linescan-profiles (atomic ratio) of the main elements along the white dissection line in Fig. 10 (c). As can be seen, a considerable reduction in Ca and Si while a rise in Mg content was noticed at the border (P1 → P2). Following, the Mg concentration reached a local maximum (P2). In the adjacent sandwiched zone where P3 was situated, the amount of Mg decreased, accompanied by a slight increase of Ca and Si contents. Remarkably, the Mg concentration rose again towards the unreacted core (P4). Basically, the elemental profiles along the dissection line agreed well with the distribution of hydration products in each sub-zone, as observed Fig. 10.

Fig. 12 gives a close-up HAADF image of a representative region in Fig. 10 (c), along with its corresponding main element mappings. Magnesium was confined within the perimeter of original slag particle and cannot enter the surrounding matrix. A higher Mg concentration was found near the perimeter and in the center. Furthermore, it appeared that Al^{3+} ion was distributed evenly across the whole area, consistent with the EDS linescan results depicted in Fig. 11.

Regarding the Ca^{2+} and Si^{4+} ions, they can readily be dissolved and transported into the cement matrix because of their high mobility. These ions played a crucial role in the formation of C−(A)–S–H gel phase as outer products. Consequently, a significant deficiency of Ca and Si was revealed at the border. With the advancement of reaction front, some Ca^{2+} and Si^{4+} ions were entrapped in the rim, participating into the precipitation of the gel phase in the sandwiched zone.

3.3. Large slag grains

In these several decades old concrete samples, partially hydrated large slag grains were frequently visible (purple-circled in Fig. 9). These grains can be recognized by hydrated thick rims and unhydrated cores, which presented dark and bright colorations, respectively. Overall, hydrated rims were developed irregularly, and their thickness varied considerably. Within the rim, the area near the boundary showed a dark coloration with a lower average atomic number (rich in Mg), while the adjacent sandwiched zone exhibited a less dark coloration with a higher mean atomic number (rich in Ca and Si). When moving inward further, a new dark region emerged (rich in Mg), which was connected with the unreacted core directly. Apart from the unhydrated core, the zonation

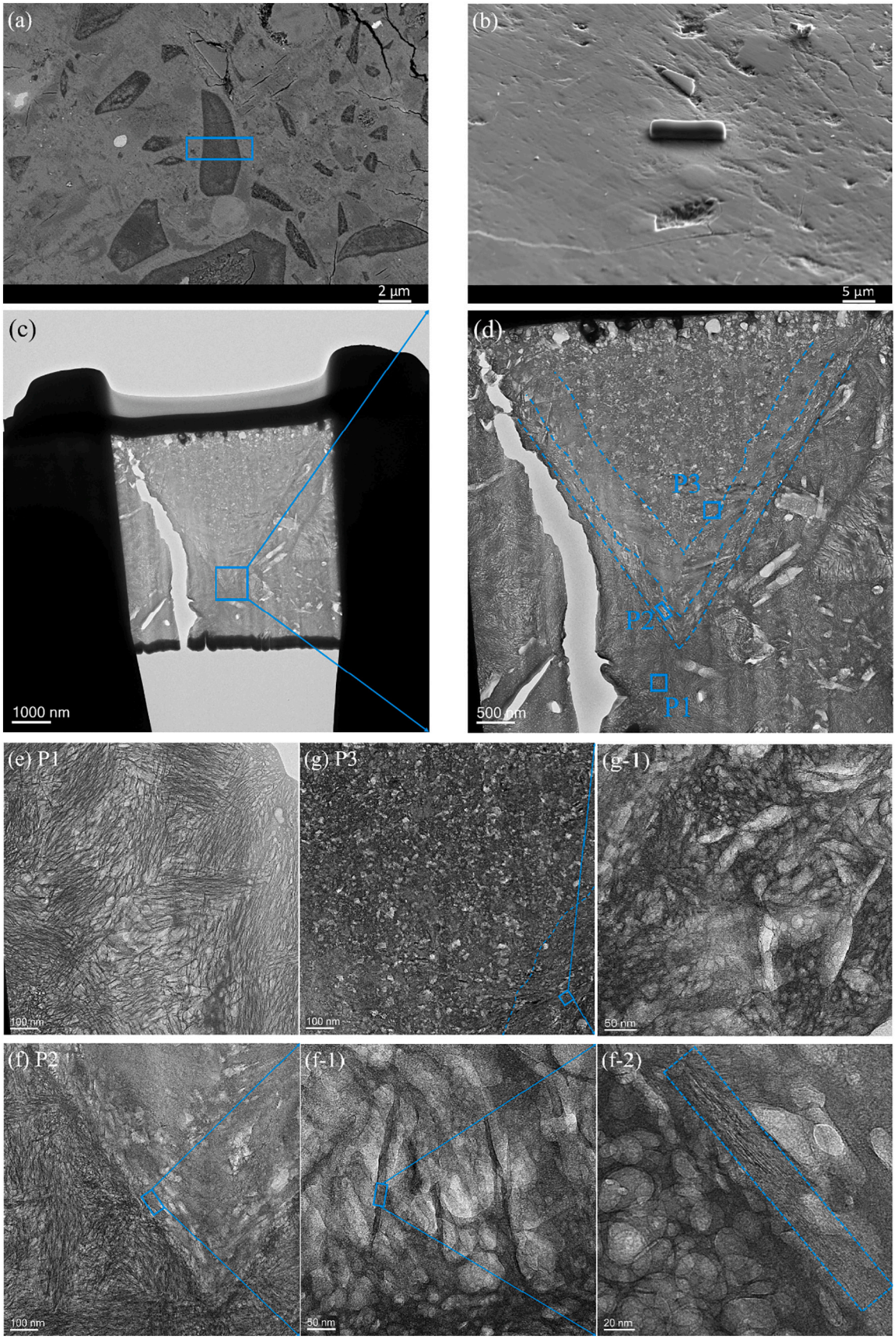

Fig. 7. TEM analysis of hydrates in an area with entire Mg occupying; (a) BSE image of the interested area; (b) Coating the area with platinum cover; (c) The overall morphology of vertical section of the target area; (d) Magnified image of the area marked in (c); (e) Magnified image of the area marked as P1 in (d); (f) Zoomed in image of the area marked as P2 in (d); (f-1) Zoomed in image of the squared region indicated in (f); (f-2) High resolution lattice fringe image of the phase marked in (f-1); (g) Magnified image of the area marked as P3 in (d); (g-1) Zoomed in image of the squared region indicated in (g).

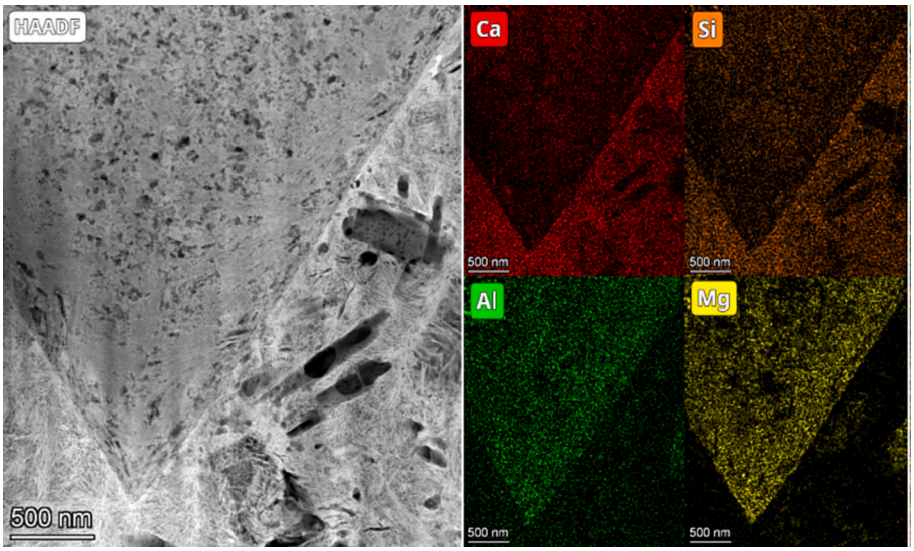

Fig. 8. The marked area in Fig. 7 illustrated by HAADF micrograph and its main element mappings. Left: HAADF micrograph; Middle top and bottom: Ca and Al mappings; Right top and bottom: Si and Mg mappings.

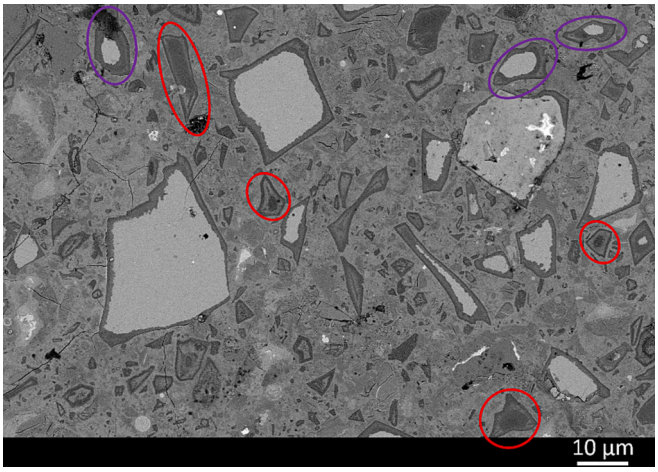

Fig. 9. A representative BSE micrograph of the microstructure.

within the rims of partially hydrated large slag grains was exactly the same to medium-sized slag particles.

3.3.1. *Multiple SEM-BSE observations*

Two representative examples encircled as 4 and 5 were displayed in Fig. 4. Within the rims, three sub-zones can be identified by two grey pixel values. It was important to note that this elemental distribution pattern was retained even as the area of unreacted cores gradually reduced with polishing.

3.3.2. *In-situ observations with TEM*

The target area, indicated by the rectangle in Fig. 2 (a), was employed as an example of a partially hydrated large slag grain for TEM analysis. Fig. 13 (a) illustrates the overview of the interested area beneath the platinum cover. The border separating the inner and outer products of slag grain was clearly noticed. A magnified image of the selected area was elaborated in Fig. 13 (b), where fibrous C−(A)–S–H gel phase was noted in the bottom-right corner of the graph. Additionally, a close-up view of the area marked as P1 at a higher magnification was displayed in Fig. 13 (c). Along the initial perimeter (P2), a zoomed in image was given in Fig. 13 (d). Massive lath-like hydrotalcite-like crystals accumulated here, with ordered atomic planes stacking implied by fringes in Fig. 13 (d-1).

When moving inside to the sandwiched zone (P3), the fibrous morphology of the gel phase was seen (Fig. 13 (e)). On the left side of Fig. 13 (f), the opaque part was considered to be the unhydrated slag core. Notably, a coarse texture was detected to surround the unreacted center (P4).

Fig. 14 reports the EDS linescan-profiles (atomic ratio) of elements along the white dissection line in Fig. 13 (a). A notable decrease in Ca and Si contents while increase in Mg concentration was found at the border (P1 → P2). On the contrary, in the sandwiched zone (P3), there was an increase in Ca and Si concentrations for the formation of C−(A)–S–H gel phase. As penetrating further towards the core where P4 was situated, a new Mg-rich region occurred connected with the unhydrated core.

Fig. 15 gives the HAADF micrograph of a representative region extracted from Fig. 13 (a), along with its corresponding main element mappings. Magnesium was distributed within the original slag grain perimeter. Ca and Si ions dissolved at the border had migrated out, leaving the boundary enriched in Mg. Moving inside to the sandwiched zone, the concentrations of Ca and Si increased while the Mg content reduced. As for aluminum, it occupied the rim and unhydrated core without any obvious enrichment. Overall, the elemental profiles along the dissection line (Fig. 14) agreed well with this element mappings.

Comparing the cases analyzed in Sections 3.2 and 3.3, it was noticed that a zonation with three sub-zones, i.e., hydrotalcite-like crystal near the boundary + C−(A)–S–H gel phase in the sandwiched zone + Mg-rich area in the core, were applicable for the hydration of both medium- and large-sized slag grains. One should keep in mind that it was commonly difficult for large slag grains to reach full hydration potential, thus unhydrated remnants can be observed in the centers surrounded by the Mg-rich area.

4. Discussion

It is worth noting that all microscopical techniques, such as SEM and TEM, only provide a 2-dimensional view of a 3-dimensional microstructure. The author in [19] had already well demonstrated the consequences of this fact. To overcome this challenge, the authors of this paper combined multiple SEM-BSE and in-situ TEM observations, and provided a 3-dimensional insight into the distribution patterns of inner products of slag. In the rims, hydrates located in different sub-zones exhibited different grey pixel values (SEM), as well as intrinsically

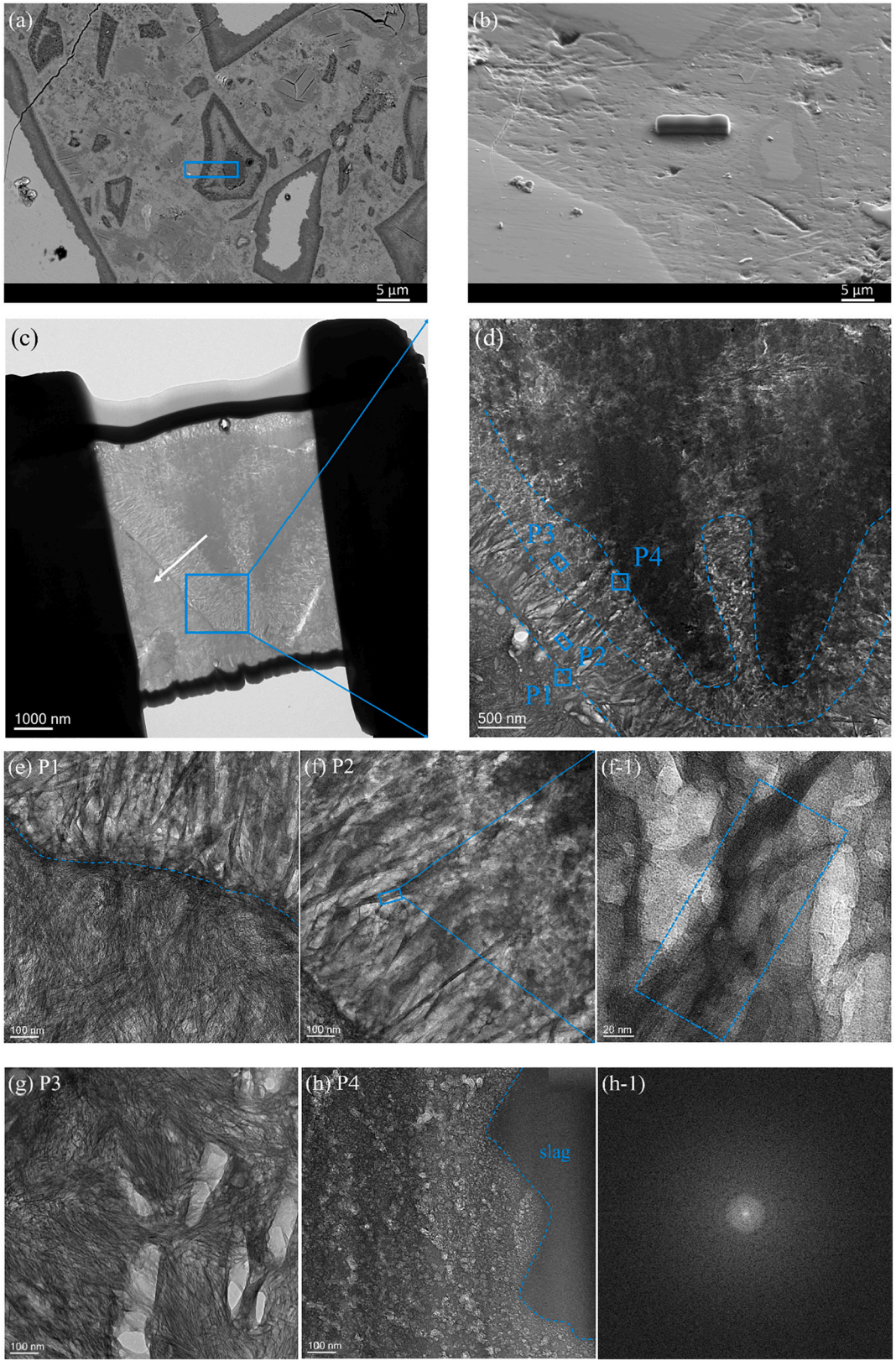

Fig. 10. TEM analysis of inner hydration products of a representative slag grain; (a) BSE image of the interested area; (b) Coating the area with platinum cover; (c) The overall morphology of hydrates beneath the platinum cover; (d) Magnified image of the area marked in (c); (e) Magnified image of the area marked as P1 in (d); (f) Zoomed in image of the area marked as P2 in (d); (f-1) High resolution lattice fringe image of the phase marked in (f); (g) Magnified image of the area marked as P3 in (d); (h) Zoomed in image of the area marked as P4 in (d); (h-1) The fast Fourier transform of phases in this region.

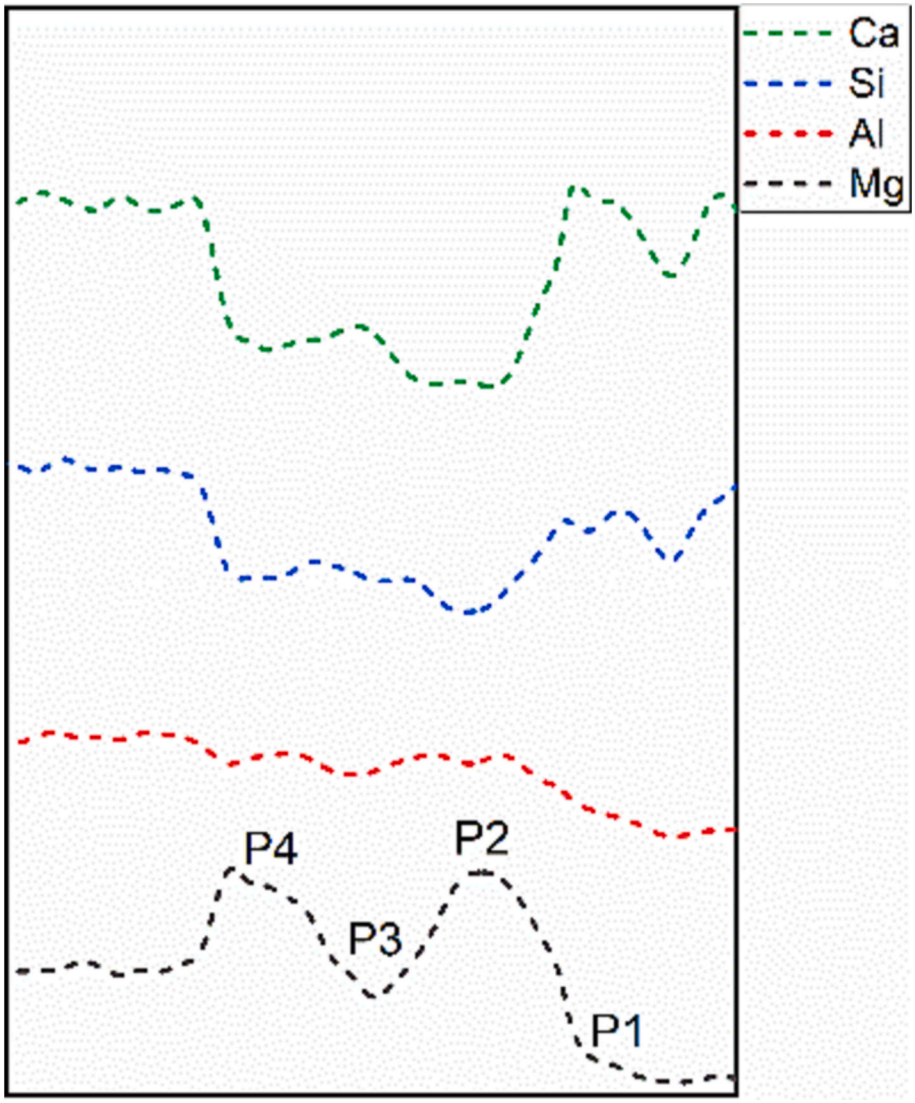

Fig. 11. Linescan-profiles of Ca, Si, Al and Mg along the white dissection line shown in Fig. 10 (c).

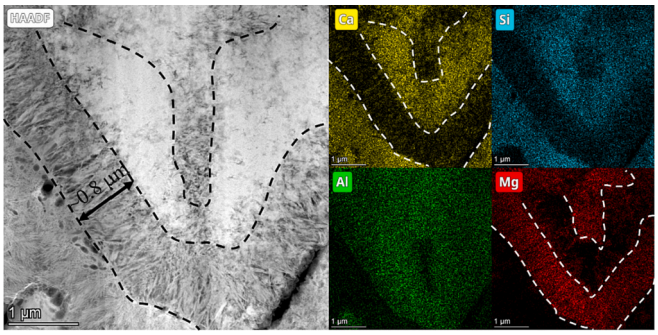

Fig. 12. A representative region in Fig. 10 (c) presented by HAADF image and its main element mappings. Left: HAADF micrograph; Middle top and bottom: Ca and Al mappings; Right top and bottom: Si and Mg mappings.

different morphologies and compositions (TEM).

Fig. 16 depicts a schematic illustration of the 3-dimensional distribution patterns of hydrates in the slag rims, which are dependent on the original sizes of parent slag particles. A detailed comparison of each pattern was reported in the Table 1 below. For fully hydrated small slag grains, lath-like, well-crystalline hydrotalcite-like crystal precipitated, grew, and accumulated near the boundary, forming a layer with a thickness slightly >0.5 µm. The magnesium, even when released in the center, can diffuse towards the boundary (concentration difference), participating in the aging of hydrotalcite-like phase. For Ca^{2+} and Si^{4+} ions dissolved at the border, they migrated into cement matrix, contributing to the formation of homogeneous, dense, and fiber-like C–(A)–S–H gel phase (outer products) with Ca/Si and Al/Si atomic ratios at ~1.10 and ~0.17, respectively. Some of the Ca^{2+} and Si^{4+} ions dissolved in the middle can also move outside into the matrix owing to their high mobility, passing through the interlayer space of hydrotalcite-like phase precipitated along the boundary. This process was driven by the concentration difference between the interior and exterior of the slag particle. For those ions trapped in the center, they took part in the local formation of fibrous gel phase. Eventually, a concentration equilibrium between cement matrix and grain core was reached, as evidenced by the similar grey-scale coloration and Ca/Si atomic ratio of the gel phases.

The larger the size of a slag grain, the harder it was to reach a full hydration. It can probably be attributed to the lack of alkaline source and/or limited space for the growth of hydrates [21,22]. Meanwhile, it was also difficult for the newly released magnesium ion from the reaction front to reach the boundary due to its low mobility [20] and the increased migration distance. Therefore, it accumulated locally to form a new Mg-rich zone. For a totally hydrated grain, the Mg-rich region

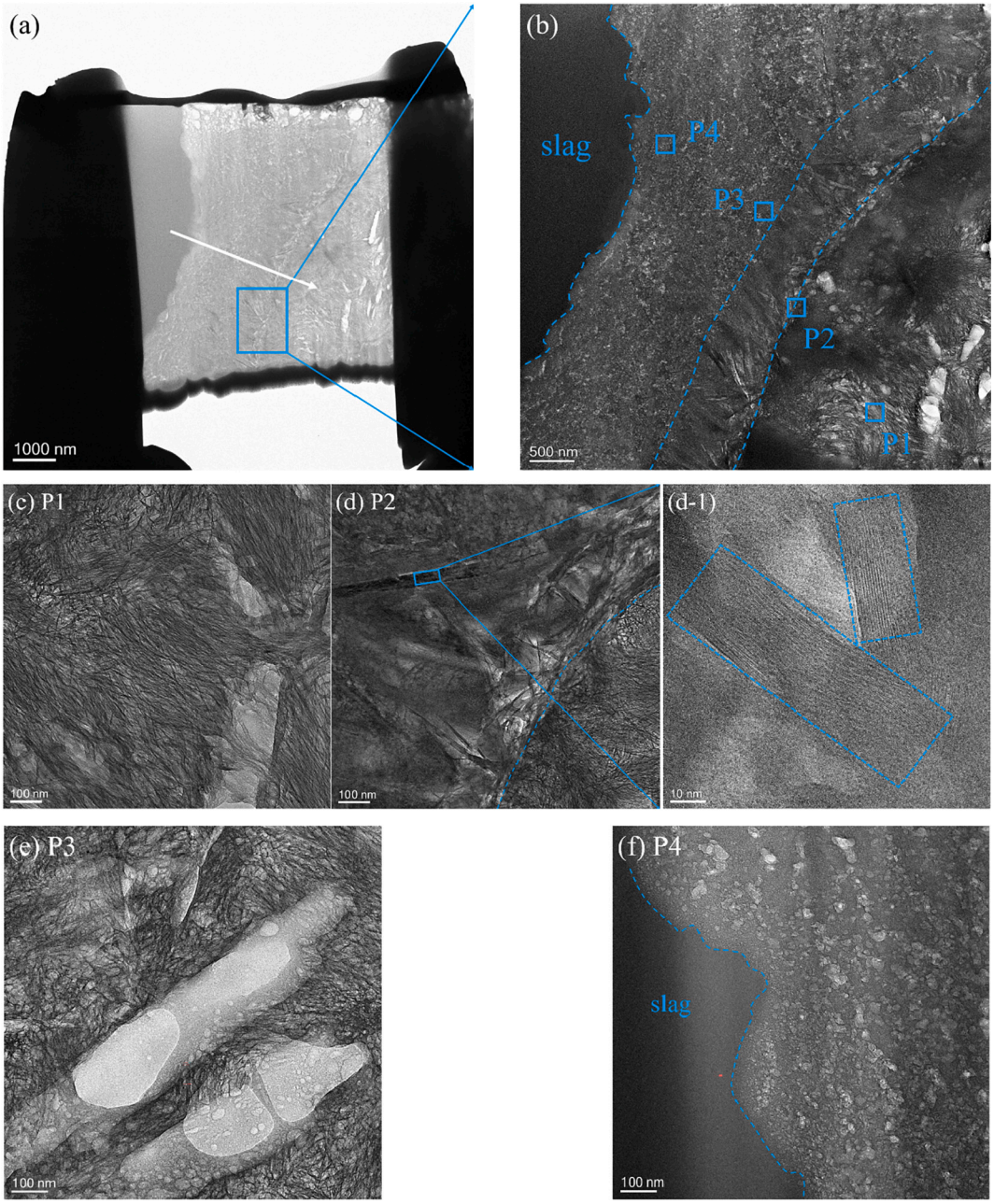

Fig. 13. TEM analysis of hydrates within the rim of a partially hydrated large slag grain; (a) The overall morphology of hydrates beneath the platinum cover; (b) Magnified image of the area marked in (c); (c) Zoomed in image of the area marked as P1 in (b); (d) Magnified image of the area marked as P2 in (b); (d-1) High resolution lattice fringe image of the phase marked in (d); (e) Magnified image of the area marked as P3 in (b); (h) Zoomed in image of the area marked as P4 in (b).

occupied the center; as for a partially hydrated one, it was connected with the unreacted slag core. Fibrous C−(A)–S–H gel phase existed in the sandwiched zone between these two magnesium-rich zones. Newly dissolved Ca^{2+} and Si^{4+} ions from the reaction front would diffuse to the sandwiched zone due to concentration differences, as well. Notably, medium- and large-sized slag grains exhibited a similar distribution pattern of hydrates, and thus were summarized together in this study.

In the previous work of [18], it was concluded that when the rim was thick enough (typically >5 μm), a new Mg-rich region started to occur locally. In other words, the maximum diffusion distance of magnesium was <5 μm. However, this value was only determined solely based on 2-dimensional SEM imaging and may not be entirely accurate. As explained in [19], sections through slag grains were generally not be equatorial, which led to an overestimation of the thickness of slag rims.

Although Mg accumulated in the new Mg-rich area, no lath-like morphology was observed in this sub-zone in both cases analyzed in Sections 3.2 and 3.3. Also, no diffraction spot was seen in the fast Fourier transform, suggesting that the phases precipitated here were disordered. In a related study [23], the authors adopted FIB to mill slag particles and investigated the dissolution and hydration of single micron-sized slag grain. They found that pH strongly affected the dissolution rate of slag and the morphology of hydrates. Large crystalline platelets, most likely to be hydrotalcite-like phase [24], was only observed at high OH- ion concentrations (> 1.0 M, i.e., pH > 14). The authors attributed this observation to the pH-dependent solubility of Mg [25]. In the dissolution process initiated at the surface of slag particles in our study, the pH of pore solution was ~13.0 [26,27]. The precipitation of platelet-like hydrotalcite-like phase at this pH was also confirmed in [28]. However, note that the pH of pore solution gradually decreased with the extension of curing [27]. Furthermore, for continues dissolution, OH^-

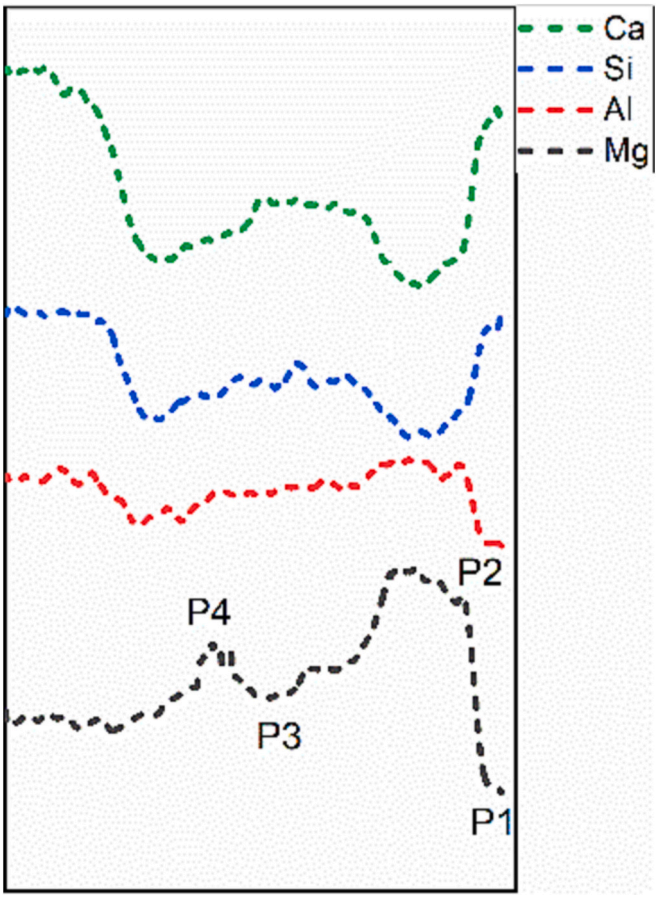

Fig. 14. Linescan-profiles of Ca, Si, Al and Mg along the white dissection line shown in Fig. 13 (a).

ion was required to migrate from pore solution to the surface of unhydrated slag core, where the local internal pH was challenging to determine. Nonetheless, this local pH was most probably lower than the bulk pH of pore solution owing to the cycle dissolution-precipitation occurring in the rim [29]. Additionally, it was worthwhile to mention that space should not be a controlling factor as the inner hydration products mainly occupied the original area of slag particle, and secondary hydrates did not require extra space for precipitation and growth.

Based on the findings in [30], it was observed that at a pH of approximately 9.0, the Mg/Al atomic ratio of synthetic hydrotalcite crystal did not go up linearly with the increasing Mg^{2+} content in the solution. Conversely, increasing the pH of solution led to enhanced Mg^{2+} incorporation into hydrotalcite framework during co-precipitation. As reported in [31], when the pH of solution dropped to <9.0, hydrotalcite crystal was not stable anymore. Mg^{2+} ion started to leach out accompanied by the formation of gibbsite. It is well accepted that aluminum hydroxides can precipitate at a relatively low pH, i.e., <5.0 [32]. In contrast, magnesium can only develop hydroxide precipitate when the pH exceeds 10.0 [33]. Therefore, although the metal-oxygen bonds existing in the network structure of slag were disrupted and Mg^{2+} ions were released locally, the low internal alkaline environment hampered the formation of lath-like hydrotalcite-like crystal. It was also reasonable to assume that the phases exhibiting a coarse and rough texture were probably associated with the formation of Mg-containing species (or the precursor of hydrotalcite-like crystal) and gibbsite.

Moreover, note that no trace of magnesium can be detected in the middle of small slag particle. However, in the sandwiched zone of medium and large slag grains, in addition to the precipitation of C–(A)–S–H gel phase, a certain amount of Mg was detected in this area (Fig. 11 and 15). It was reasonable as small slag grains reacted fast at an early age, facilitating the relatively easy diffusion of magnesium. However, the microstructure of cement matrix became denser at the later stage of hydration, and there was little pore and pore solution left for its transportation. As mentioned earlier, hydrotalcite-like crystal was not formed in the center and Mg probably existed in a free state. Therefore, magnesium can diffuse to the sandwiched zone because of concentration difference.

As proposed in [19], large slag particles had a higher likelihood of being sectioned. When cut along the unreacted center as the case demonstrated in Section 3.3, the distribution pattern of hydrates can be observed properly. However, when sectioned along different sub-zones in the rim (Fig. 17), some misleading results may be yielded. For example, when sectioned along line 1, this partially reacted large slag grain would appear as a 'small' area with a uniformly dark coloration, similar to the case analyzed in Section 3.1.2.2. Along dissection line 2, it would be easily mistaken for a completely hydrated 'small' slag particle exhibiting two sub-zones. However, some magnesium can be detected in the center of this 'small' grain. This served as the main clue to distinguish a real small slag grain and a small area cut from the rim along a partially hydrated slag particle. When cut along line 3, three sub-zones would be found, like the case investigated in Section 3.2.2. Under this circumstance, there were currently no clues available to identify whether unhydrated slag remnants remained below the sample surface

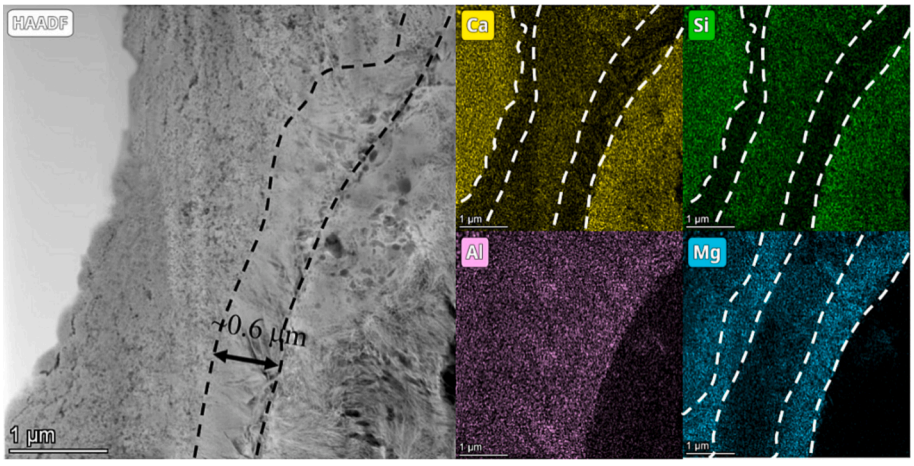

Fig. 15. A representative region extracted from Fig. 13 presented by HAADF micrograph and its main element mappings. Left: HAADF micrograph; Middle top and bottom: Ca and Al mappings; Right top and bottom: Si and Mg mappings.

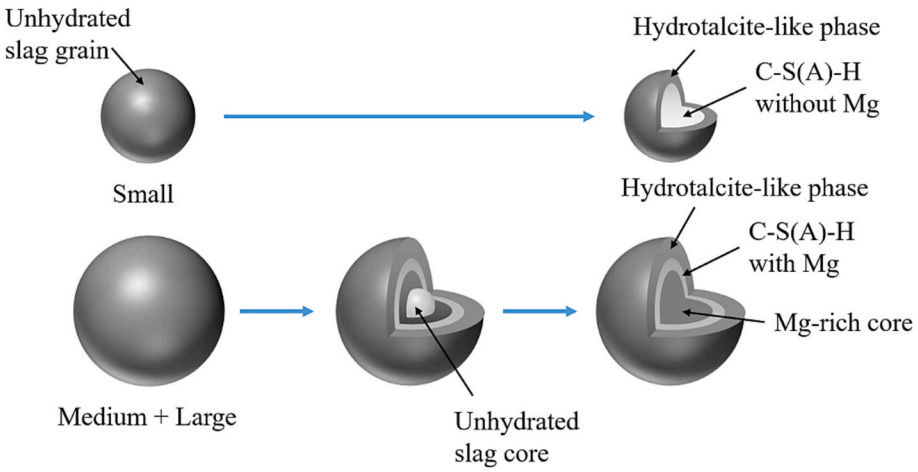

Fig. 16. A schematic illustration of 3-dimensional distribution patterns of hydrates in the slag rims with different original sizes.

Table 1
A detailed comparison of each pattern.

Group	Sub-zones	Comments
Small	2	Hydrotalcite-like crystal near the boundary + C−(A)–S–H gel phase in the core (without Mg)
Medium/ Large	3	Hydrotalcite-like crystal near the boundary + C−(A)–S–H gel phase (with Mg) in the sandwiched zone + Mg-rich species in the core

or not.

5. Conclusions

Combining multiple SEM-BSE and in-situ TEM observations together, the authors in this paper provided a comprehensive 3-dimensional insight into the distribution patterns of inner products of slag. Within the rims, hydrates located in different sub-zones exhibited different grey pixel values (SEM), as well as intrinsically different morphologies and compositions (TEM).

- For fully hydrated small slag grains, two distinct sub-zones were formed in the rims. Lath-like, well-crystalline hydrotalcite-like crystals were found to precipitate, grow, and accumulate near the boundary, forming a layer with a thickness slightly exceeding 0.5 μm. In the center, entrapped calcium and silicon played roles in the formation of a homogeneous and fibrous C−(A)–S–H gel phase. The concentration equilibrium between cement matrix and grain core led to the establishment of a similar grey pixel value (SEM) and Ca/Si atomic ratio of gel phase at ~1.10 (TEM).
- As for medium- and large-sized slag grains, three sub-zones became visible. Hydrotalcite-like phase was enriched near the boundary, followed by a sandwiched area abundant in fibrous C−(A)–S–H gel phase. Due to the low mobility and increased migration distance, newly released magnesium from reaction front accumulated locally to form a new Mg-rich region.
- The low internal alkaline environment hampered the formation of hydrotalcite-like crystal in the additional Mg-rich region, which exhibited a coarse and rough texture. Magnesium dissolved in this area was able to diffuse into the sandwiched zone owing to the concentration difference. However, no trace of magnesium can be detected in the center of small slag particle. It was the main clue to distinguish a real small slag grain and a small area cut from the rim along a partially hydrated slag particle.

Our findings suggest that it is the size of a slag grain and the low mobility of magnesium that determine the 3-dimensional distribution patterns of inner hydration products of slag. Considering that none of the existing hydration models relates the original slag size to the generated phase zoning, the results in this paper would be beneficial for slag hydration modelling. Besides, it should be emphasized that well crystalline hydrotalcite-like crystals occupy the boundary upon hydration of slag grains, with a thickness of ~0.5 μm. Therefore, the contribution of

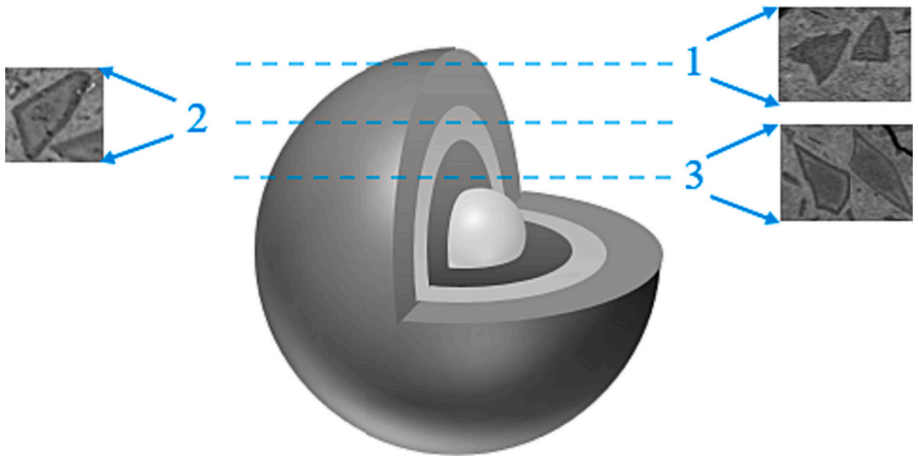

Fig. 17. A schematic illustration of sections along different sub-zones of thick rim around a partially hydrated large slag grain.

hydrotalcite-like cannot be overlooked, especially for systems with a high slag substitution level. Its massive formation, growth, and aging partially explains the excellent performance of blended cements in both strength and durability aspects. This phase exhibits better micro-mechanical properties, including elastic modulus and hardness, than C−(A)–S–H gel phase [34]. Furthermore, hydrotalcite-like phase can increase the durability through absorbing various harmful species as interlayer ions [35–40].

Meanwhile, it is worthwhile to mention that not all magnesium released by slag participate into the formation of hydrotalcite-like crystal, especially for those dissolved in the core of medium- and large-sized slag grains. They mainly exist as a free state or in the precursor of hydrotalcite-like crystal. Thus, BSE image analysis method would overestimate the quantitative content of hydrotalcite-like crystal produced in slag-containing systems.

CRediT authorship contribution statement

Yu Zhang: Conceptualization, Formal analysis, Funding acquisition, Investigation, Methodology, Writing – original draft, Writing – review & editing. **Oğuzhan Çopuroğlu:** Conceptualization, Methodology, Supervision, Writing – review & editing.

Declaration of competing interest

The authors declare no conflict of interest.

Data availability

Data will be made available on request.

Acknowledgements

Fundamental Research Funds for the Central Universities (Grant Number RF1028623287) is gratefully acknowledged for the financial support. Bart Hendrix (Microlab, TU Delft) shared the samples from field for investigation, and authors would also like to thank him. Xuefeng Zhang from Shiyanjia Lab (www.shiyanjia.com) is greatly appreciated for his help on FIB-SEM system.

References

[1] Y. Yang, K. Raipala, L. Holappa, Ironmaking, in: Treatise on Process Metallurgy, Elsevier, 2014.
[2] I. Sohn, D.J. Min, A review of the relationship between viscosity and the structure of calcium-silicate-based slags in ironmaking, Steel Res. Int. 83 (7) (2012) 611–630.
[3] M.C. Juenger, R. Snellings, S.A. Bernal, Supplementary cementitious materials: new sources, characterization, and performance insights, Cem. Concr. Res. 122 (2019) 257–273.
[4] E. Özbay, M. Erdemir, H.İ. Durmuş, Utilization and efficiency of ground granulated blast furnace slag on concrete properties – a review, Constr. Build. Mater. 105 (2016) 423–434.
[5] H.F. Taylor, Cement Chemistry Vol. 2, Thomas Telford London, 1997.
[6] J. Skibsted, R. Snellings, Reactivity of supplementary cementitious materials (SCMs) in cement blends, Cem. Concr. Res. 124 (2019), 105799.
[7] K.C. Newlands, et al., Early stage dissolution characteristics of aluminosilicate glasses with blast furnace slag- and fly-ash-like compositions, J. Am. Ceram. Soc. 100 (5) (2017) 1941–1955.
[8] R. Snellings, C. Jantzen, Solution-controlled dissolution of supplementary cementitious material glasses at pH 13: the effect of solution composition on glass dissolution rates, J. Am. Ceram. Soc. 96 (8) (2013) 2467–2475.
[9] M. Zajac, et al., Late hydration kinetics: indications from thermodynamic analysis of pore solution data, Cem. Concr. Res. 129 (2020), 105975.
[10] W. Chen, H. Brouwers, The hydration of slag, part 2: reaction models for blended cement, J. Mater. Sci. 42 (2) (2007) 444–464.
[11] R. Taylor, I. Richardson, R. Brydson, Composition and microstructure of 20-year-old ordinary Portland cement–ground granulated blast-furnace slag blends containing 0 to 100% slag, Cem. Concr. Res. 40 (7) (2010) 971–983.
[12] I. Richardson, G. Groves, Microstructure and microanalysis of hardened cement pastes involving ground granulated blast-furnace slag, J. Mater. Sci. 27 (22) (1992) 6204–6212.
[13] I. Richardson, G. Groves, The structure of the calcium silicate hydrate phases present in hardened pastes of white Portland cement/blast-furnace slag blends, J. Mater. Sci. 32 (18) (1997) 4793–4802.
[14] I. Richardson, Tobermorite/jennite-and tobermorite/calcium hydroxide-based models for the structure of CSH: applicability to hardened pastes of tricalcium silicate, β-dicalcium silicate, Portland cement, and blends of Portland cement with blast-furnace slag, metakaolin, or silica fume, Cem. Concr. Res. 34 (9) (2004) 1733–1777.
[15] I. Richardson, S. Li, Composition and structure of an 18-year-old 5M KOH-activated ground granulated blast-furnace slag paste, Constr. Build. Mater. 168 (2018) 404–411.
[16] H. Ye, Nanoscale attraction between calcium-aluminosilicate-hydrate and Mg-Al layered double hydroxides in alkali-activated slag, Mater. Charact. 140 (2018) 95–102.
[17] B. Li, Q. Li, W. Chen, Spatial zonation of a hydrotalcite-like phase in the inner product of slag: new insights into the hydration mechanism, Cem. Concr. Res. 145 (2021), 106460.
[18] Y. Zhang, O. Çopuroğlu, Role of the grain size on the hydration characteristics of slag in an aged field concrete, Cem. Concr. Res. 162 (2022), 106985.
[19] K.L. Scrivener, Backscattered electron imaging of cementitious microstructures: understanding and quantification 26 (8) (2004) 935–945.
[20] Q. Feng, E. Lachowski, F. Glasser, Densification and migration of ions in blast furnace slag-portland cement pastes, in: MRS Online Proceedings Library Archive 136, 1988.
[21] W.J. Lee, M.H. Hon, Space-limited crystal growth mechanism of TiO_2 films by atomic layer deposition, J. Phys. Chem. C 114 (15) (2010) 6917–6921.
[22] A. Machner, et al., Limitations of the hydrotalcite formation in Portland composite cement pastes containing dolomite and metakaolin, Cem. Concr. Res. 105 (2018) 1–17.
[23] P. Suraneni, M. Palacios, R.J. Flatt, New insights into the hydration of slag in alkaline media using a micro-reactor approach, Cem. Concr. Res. 79 (2016) 209–216.
[24] D.M. Roy, E. Sonnenthal, R. Prave, Hydrotalcite observed in mortars exposed to sulfate solutions, Cem. Concr. Res. 15 (5) (1985) 914–916.
[25] S. Song, H.M. Jennings, Pore solution chemistry of alkali-activated ground granulated blast-furnace slag, Cem. Concr. Res. 29 (1999) 159–170.
[26] A. Vollpracht, et al., The pore solution of blended cements: a review, Mater. Struct. 49 (2016) 3341–3367.
[27] A. Schöler, et al., Early hydration of SCM-blended Portland cements: a pore solution and isothermal calorimetry study, Cem. Concr. Res. 93 (2017) 71–82.
[28] R. Snellings, T. Paulhiac, K. Scrivener, The effect of Mg on slag reactivity in blended cements, Waste Biomass Valoriz. 5 (2014) 369–383.
[29] R.G. Pike, D. Hubbard, Increased chemical reactivity of the surface compared with that in the bulk volume of Britton-Robinson universal buffers, J. Res. Natl. Bur. Stand. 59 (6) (1957) 411–414.
[30] J.Y. Lee, et al., Synthesis of hydrotalcite type layered double hydroxide with various Mg/Al ratio and surface charge under controlled reaction condition, Appl. Clay Sci. 134 (2016) 44–49.
[31] C. Foster, et al., Hydrotalcite colloidal stability and interactions with uranium(VI) at neutral to alkaline pH, Langmuir 38 (8) (2022) 2576–2589.
[32] W. Mchardy, A. Thomson, Conditions for the formation of bayerite and gibbsite, Mineral. Mag. 38 (295) (1971) 358–368.
[33] C.F. Baes, R.E. Mesmer, Hydrolysis of Cations, Wiley, New Jersey, 1976.
[34] Y. Zhang, et al., Micro-mechanical properties of slag rim formed in cement–slag system evaluated by nanoindentation combined with SEM, Materials 15 (18) (2022) 6347.
[35] Z. Yang, H. Fischer, R. Polder, Synthesis and characterization of modified hydrotalcites and their ion exchange characteristics in chloride-rich simulated concrete pore solution, Cem. Concr. Compos. 47 (2014) 87–93.
[36] M. Balonis, et al., Impact of chloride on the mineralogy of hydrated Portland cement systems, Cem. Concr. Res. 40 (7) (2010) 1009–1022.
[37] J. Xu, Q. Tan, Y. Mei, Corrosion protection of steel by Mg-Al layered double hydroxides in simulated concrete pore solution: effect of SO_4^{2-}, Corros. Sci. 163 (2020), 108223.
[38] S. Walspurger, et al., High CO_2 storage capacity in alkali-promoted hydrotalcite-based material: in situ detection of reversible formation of magnesium carbonate, Chem. Eur. J. 16 (42) (2010) 12694–12700.
[39] Y. Zhang, O. Çopuroğlu, The role of hydrotalcite-like phase and monosulfate in slag cement paste during atmospheric and accelerated carbonation, Cem. Concr. Compos. 132 (2022), 104642.
[40] Y. Zhang, et al., Effect of MgO content on the quantitative role of hydrotalcite-like phase in a cement-slag system during carbonation, Cem. Concr. Compos. 134 (2022), 104765.